

Comparing Quantum Annealing and Spiking Neuromorphic Computing for Sampling Binary Sparse Coding QUBO Problems

Kyle Henke^{*†1}, Elijah Pelofske^{*†1}, Garrett Kenyon^{§1}, and Georg Hahn^{¶2}

¹Los Alamos National Laboratory, CCS-3 Information Sciences

²Harvard University, T.H. Chan School of Public Health

Abstract

We consider the problem of computing a sparse binary representation of an image. To be precise, given an image and an overcomplete, non-orthonormal basis, we aim to find a sparse binary vector indicating the minimal set of basis vectors that when added together best reconstruct the given input. We formulate this problem with an L_2 loss on the reconstruction error, and an L_0 (or, equivalently, an L_1) loss on the binary vector enforcing sparsity. This yields a quadratic binary optimization problem (QUBO), whose optimal solution(s) in general is NP-hard to find. The contribution of this work is twofold. First, the method of unsupervised and unnormalized dictionary feature learning for a desired sparsity level to best match the data is presented. Second, we solve the sparse representation QUBO by implementing it both on a D-Wave quantum annealer with Pegasus chip connectivity via minor embedding, as well as on the Intel Loihi 2 spiking neuromorphic processor. On the D-Wave quantum annealer, we sample from the sparse representation QUBO using parallel quantum annealing combined with quantum evolution Monte Carlo, also known as iterated reverse annealing. On the Loihi 2 neuromorphic chip, we use a stochastic winner take all network of neurons. The solutions are benchmarked against simulated annealing, a classical heuristic, and the optimal solutions are computed using CPLEX. Iterated reverse quantum annealing performs similarly to simulated annealing, although simulated annealing is always able to sample the optimal solution whereas quantum annealing was not always able to. The Loihi 2 solutions that are sampled are on average more sparse than the solutions from any of the other methods. We demonstrate that both quantum annealing and neuromorphic computing are suitable for binary sparse coding QUBOs, and that Loihi 2 outperforms a D-Wave quantum annealer standard linear-schedule anneal, while for these types of QUBOs, iterated reverse quantum annealing performs much better than both unmodified linear-schedule quantum annealing and iterated warm starting on Loihi 2.

1 Introduction

The computation of a sparse binary reconstruction of an image is of importance whenever a full image cannot be directly observed, in which case it has to be reconstructed from a sample or projection using compressive sensing. Such scenarios occur, amongst others, in radioastronomy, molecular imaging, and image compression [51, 40].

Mathematically, we are given an overcomplete and non-orthonormal basis of $n \in \mathbb{N}$ matrices $\phi = \{\phi_1, \dots, \phi_n\}$, and we aim to infer a sparse representation of a given image \mathbf{I} . Here, an overcomplete set is defined as one that contains more functions than needed for a basis. All basis matrices as well as the image \mathbf{I} are assumed to be of equal dimensions. The task is to find the minimal set of non-zero activation coefficients \mathbf{a} that accurately reconstruct \mathbf{I} , where $\mathbf{a} \in \mathbb{B}^n$ is a binary vector of length n for $\mathbb{B} = \{0, 1\}$. We can express the computation of a sparse binary representation of the image \mathbf{I} using the basis ϕ as the minimization of the energy function

$$E(\mathbf{I}, \mathbf{a}) = \min_{\mathbf{a}} \left[\frac{1}{2} \|\mathbf{I} - \phi \mathbf{a}\|_2^2 + \lambda \|\mathbf{a}\|_0 \right], \quad (1)$$

where $\|\cdot\|_2$ is the Euclidean norm and $\|\cdot\|_0$ denotes the number of nonzero elements. The operation $\phi \mathbf{a}$ denotes the addition of all basis matrices in ϕ that correspond to an entry of 1 in \mathbf{a} . The parameter $\lambda > 0$ is a Lasso-type

*These two authors contributed equally to this work.

†Email: khenke@lanl.gov

‡Email: epelofske@lanl.gov

§Email: gkenyon@lanl.gov

¶Email: ghahn@hsph.harvard.edu

penalization parameter controlling the sparseness of the solution [50]. A large value of λ results in a more sparse solution to eq. (1), while smaller values yield denser solutions. Therefore, the parameter λ allows one to effectively balance the reconstruction error (the L_2 norm) and the number of non-zero activation coefficients (the L_0 norm). Since eq. (1) belongs to the class of 0-1 integer programming problems, finding a sparse representation falls into an NP-hard complexity class. The energy function of eq. (1) is non-convex and typically contains multiple local minima.

We investigate two types of computing models to solve the sparse representation problem given in eq. (1). The first is a D-Wave quantum annealer with chip ID `Advantage_system4.1`. Moreover, we employ the spiking neuromorphic computing processor Loihi 2 by Intel. Quantum annealing is a type of analog quantum computation that aims to use quantum fluctuations in order to search the objective function landscape of a combinatorial optimization problem for the global minimum [28, 18]. Quantum annealer devices are manufactured by D-Wave, which use superconducting flux qubits to implement quantum annealing with a transverse field Hamiltonian and have been studied for sampling a variety of problem types [27, 36]. Although current quantum annealers are subject to various sources of errors, limited coherence times, and limited hardware connectivity, there is evidence that quantum annealing can provide an advantage over classical algorithms for certain types of problems [34, 49, 31, 5]. Neuromorphic computing is a proposed computing model inspired by the human brain, which is able to complete certain learning tasks better than classical von Neumann computers [17, 48].

This article is a significant extension of [24], in which the unsupervised dictionary learning approach to generate sparse coding QUBO models was introduced for the purposes of sampling those problems on Loihi 1. The article is structured as follows. After a literature review in Section 1.1, we introduce the quantum annealing and neuromorphic computing technology we investigate in Section 2. Experimental results are presented in Section 3. The article concludes with a discussion in Section 4.

1.1 Literature review

The goal of any sparse coding method is to accurately recover an unknown sparse vector from a few noisy linear measurements. Unfortunately, this estimation problem is NP-hard in general (when formulated as 0-1 integer optimization), and it is therefore usually approached with an approximation method, such as some Lasso or orthogonal matching pursuit (OMP) [52], thus trading off accuracy for less computational complexity.

In [46], the authors investigate the suitability of sparse approximations, or also called sparse coding, to minimize an objective consisting of an error term with L_2 loss and a coefficient cost function, where sparse representations are enforced in neural systems with the help of local symmetric competitions among neurons.

A comparison of quantum computing (using the D-Wave quantum annealer) and neuromorphic computing (using the Intel Loihi spiking processor) has been investigated in [22, 23], who compare both on an identically-posed machine learning problem with respect to various metrics (power consumption, reconstruction and classification accuracy, etc). This line of research is continued in [21], who compare sparse coding solutions generated classically by orthogonal matching pursuit (OMP) with spike-based solutions obtained with the Loihi 1 neuromorphic processor. Their article investigates post-hoc normalization techniques to speed up computations on Loihi 1, optimal parameter selection, reconstruction errors, and unsupervised dictionary learning for Loihi 1 approaches and their classical counterparts.

A quantum-inspired algorithm for sparse coding is presented in [45] by formulating a general sparse coding problem as a quadratic unconstrained binary optimization (QUBO) problem suitable for approximation on current hardware such as the D-Wave quantum annealers. Similar research on regularized linear regression for sparse signal reconstruction is presented in [26], who also derive a QUBO representation and compare solutions obtained with D-Wave Advantage Systems 4.1 to OMP and conventional Lasso methods.

Two related problems, binary compressive sensing and binary compressive sensing with matrix uncertainty, are investigated in [3], though no experimental results on D-Wave devices are presented.

2 Methods

In this section we present the hardware being used in this research. After some mathematical considerations on the problem under investigation (Section 2.1), we give details on Intel’s Loihi 2 neuromorphic chip (Section 2.2), followed by some implementation details for the D-Wave quantum annealer (Section 2.3). Section 2.4 describes the classical simulated annealing implementation which we will compare against. Section 2.5 discusses the exact solution obtained with IBM’s CPLEX solver [25], which is exact and deterministic.

2.1 Binary Sparse Coding QUBOs

For both Intel’s Loihi 2 neuromorphic chip, as well as the D-Wave quantum annealer, the problem being solved has to be given as a QUBO problem. In this formulation, the observable states of any variable are 0 and 1. During the solution process, both technologies can be described as effectively treating each spin/neuron in some probabilistic combination of 0 and 1, in which the variable is both active and non-active at the same time. After the quantum annealing process or the firing process in the neural net is complete, each variable will return to one of the classical states 0 or 1.

We start by reformulating eq. (1) in QUBO form. To this end, denoting $D = \phi$ and $\mathbf{x} = \mathbf{I}$, we observe that for $\mathbf{a} \in \mathbb{B}^n$,

$$\begin{aligned} E(\mathbf{a}) &= \frac{1}{2} \|\mathbf{x} - D\mathbf{a}\|_2^2 + \lambda \|\mathbf{a}\|_0 \\ &= \frac{1}{2} \mathbf{x}^\top \mathbf{x} - \mathbf{x}^\top D\mathbf{a} + \frac{1}{2} \mathbf{a}^\top D^\top D\mathbf{a} + \lambda \sum_{i=1}^n a_i, \end{aligned}$$

where $\mathbf{a} = (a_1, \dots, a_n)$. As expected, multiplying out eq. (1) yields a quadratic form in \mathbf{a} , meaning that we can recast our objective function as a QUBO problem. For this we define the following two transformations:

$$h_i = -D_i^\top \mathbf{x} + \lambda + \frac{1}{2} D_i^\top D_i \quad (2)$$

$$Q_{ij} = \frac{1}{2} (D^\top D)_{ij} - \mathbb{I}(i = j), \quad (3)$$

where \mathbb{I} denotes the indicator function which returns 1 if and only if its argument is true, and 0 otherwise. Using eq. (2) and eq. (3), we can rewrite eq. (1) as the following QUBO,

$$H(\mathbf{h}, Q, \mathbf{a}) = \sum_{i=1}^n h_i a_i + \sum_{i < j} Q_{ij} a_i a_j \quad (4)$$

which is now in suitable form to be solved on either the Loihi 2 neuromorphic chip or the D-Wave quantum annealer.

Figure 1 shows a visual representation of both a 64 and 128 variable sparse coding QUBO as a symmetric square matrix, where the diagonal terms are the linear terms of eq. (4), and the off-diagonal terms are the quadratic variable interactions. The coefficients for each term are encoded using a colormap. Figure 1 shows that the linear terms are typically strongly positively or negatively weighted compared to the off diagonal terms.

The binary sparse coding QUBOs are constructed using the un-normalized dictionary learning introduced in [24]. In particular, the dictionary learning is performed using the classical heuristic simulated annealing using the settings that will be described in Section 2.4. As done previously [24], a single image from the standard fashion MNIST (fMNIST) data set [55] is used, where the 28x28 image is divided into 16 7x7 patches, and then a dictionary size of 64 variables is used for each of the 16 patches. We also evaluate a version where we increase the dictionary size to 128 variables, and use a patch size of 2x2 (resulting in 4 separate QUBOs).

2.2 Implementation on Loihi

This section guides through several implementation details on Intel’s Loihi 2 spiking neuromorphic chip.

2.2.1 Lateral competition

Previous work has shown that sparse coding optimization problems, such as the one we focus on in eq. (1), can be solved using the dynamics of neural networks incorporating lateral inhibition, a biologically plausible implementation of a sparse solver referred to as a locally competitive algorithm (LCA). LCA aims to find a sparse solution of eq. (1) by allowing the dynamical system to evolve to a minimum energy configuration. However, such dynamical systems are susceptible to local minima.

2.2.2 Loihi 2 Neuromorphic Chip Implementation

The Intel Loihi 2 neuromorphic processor aims to mimic the neural structure and processing methods of the human, which can be used to address specific types of computational tasks. Compared to the previous generation of the

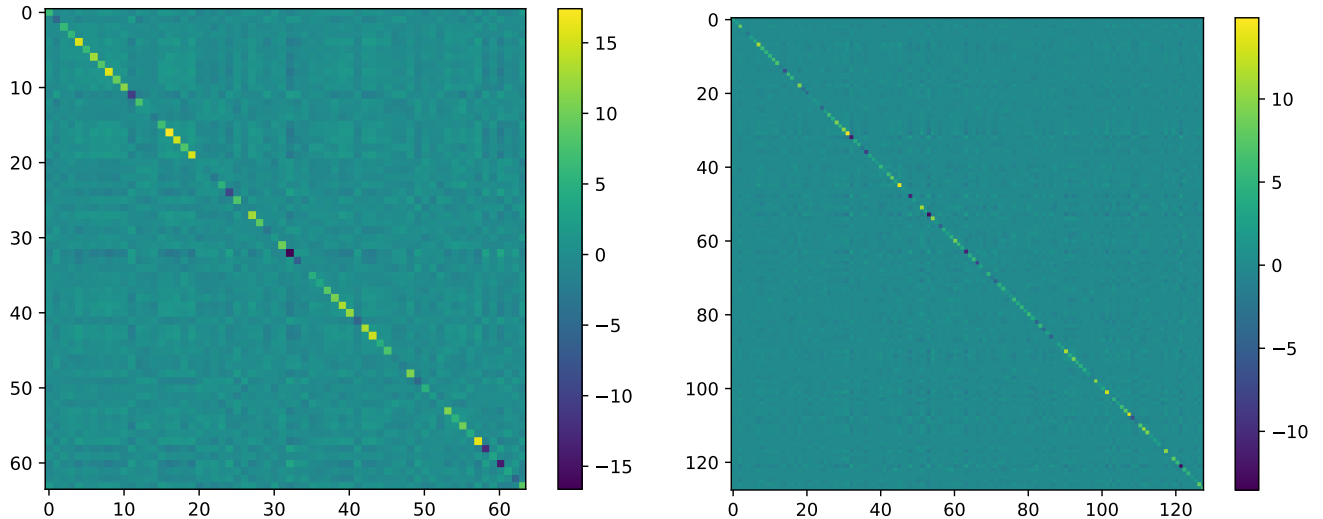


Figure 1: Colormaps of the full QUBO symmetric matrix for a (randomly chosen and representative) sparse coding QUBO with 64 variables (left) and 128 variables (right). Each heatmap corresponds to the coefficient for each of the linear terms (on the diagonal) and for each of the quadratic terms (on the off-diagonals).

Loihi processor, Loihi 2 has several expanded capabilities, namely improved manufacturing. Loihi 2 contains 1 million neurons per chip, and has about 120 million synapses.

Loihi 2 utilizes graded 8-bit spike events, which are different from the binary spike events used in Loihi 1. This change allows the processor to model neural information in a way that is closer to the biological functioning of the human brain. In particular, Loihi 1 enabled communication between artificial neurons with binary spikes. Those digital pulses represented the firing of a neuron by effectively transmitting a signal that has only two states: “on” or “off” (1 or 0). This binary approach mimics the all-or-nothing nature of neuron activity in biological brains at a fundamental level but with less granularity. With the introduction of graded 8-bit spike events instead of binary spikes, each spike can carry more nuanced information, with the intensity of the spike encoded in 8 bits.

In contrast with the Stochastic Constraint Integrate and Fire (SCIF) neuron model that was implemented in [24] for Loihi 1, using the new functionality of Loihi 2, we are able to deploy a Non-equilibrium Boltzmann (NEBM) neuron model specifically designed to address optimization problems such as the QUBO problem. This model is inspired by the principles of statistical mechanics and thermodynamics, particularly the concept of a non-equilibrium steady state in systems that are driven by external forces.

The NEBM neuron model diverges from traditional artificial neuron models by incorporating the dynamics of non-equilibrium systems. In typical computational models like the Boltzmann machine, neurons are treated as binary units that reach an equilibrium state where the probability distribution of their states follows the Boltzmann distribution. In contrast, the NEBM model operates under non-equilibrium conditions, meaning the system does not settle into a thermal equilibrium but is instead continuously driven by external inputs or energy sources. Unlike equilibrium models where state transitions depend solely on minimizing the system’s energy, NEBM incorporates dynamics where transitions also depend on external driving forces. This allows the system to explore more of the solution space and potentially escape local minima more effectively. In NEBM, energy is not conserved but dissipated due to the system’s open and driven nature. This aspect is crucial for implementing effective annealing processes, where the system can cool down and stabilize towards a solution of the optimization problem. The NEBM model also includes time as a critical factor, with the system’s state evolving over time rather than settling into a static equilibrium. This temporal aspect allows for dynamic updating rules that can be tuned for faster convergence or better exploration of the solution space.

For the task of optimizing a QUBO problem using the NEBM neuron model, the first step is to map each variable in the QUBO to a neuron in the NEBM. The interactions defined in the QUBO matrix are translated into synaptic connections between these neurons. Similar to simulated annealing, the NEBM model can implement a form of dynamic annealing where the system gradually stabilizes by reducing the impact of external drives and allowing the system to settle into a low-energy configuration that corresponds to an optimal or near-optimal solution of the QUBO problem. The system is initialized in a non-equilibrium state and evolves according to specified dynamics, driven by both internal neuronal computations and external inputs. These dynamics are designed to reduce the

overall energy defined by the QUBO, but with considerations for non-equilibrium behavior that allows exploration. The NEBM approach can be programmed onto neuromorphic hardware like Loihi 2, which can mimic these dynamic and non-equilibrium processes efficiently, using spiking neural networks.

The exact hyperparameters used to run Loihi 2 are as follows. The neuron model is set to `nebm-sa-refract`. The annealing schedule is linear. The maximum temperature is 15, and the minimum temperature is 1, and the number of steps per temperature is 20, with temperature delta set to 1. The parameter `refract_scaling` is set to a random integer between 4 and 8, and `refract` is set to a random integer between 5 and 10. The `refract_counter` is set to 0.

An additional technique that we introduce is *iterated warm starting* on Loihi 2; we initialize with a standard run, then take the best found solution in that run and initialize the next run with that solution. This is then repeated a total of 100 times. The initial run is initialized with a random binary vector. As far as we are aware, this is the first description and assessment of using warm starting iteratively on a spiking neuromorphic processor.

2.3 Quantum Annealing Implementation

This section gives some background on the D-Wave quantum device we employ to minimize the sparse coding QUBO of eq. (4).

Quantum annealing is a type of analog quantum computation that generally has the goal of computing low energy states in a physical system that correspond to low energy states of a classical spin system [28, 18, 47, 41, 15]. A review of quantum annealing can be found in [20]. D-Wave manufactures quantum annealers using superconducting flux qubits [27, 36], several generations of which have been utilized in a large number of studies of different optimization problems and physical spin systems [30, 19, 7, 53, 6].

The D-Wave quantum annealer is designed to minimize QUBO problems, given by functions of the form of eq. (4). In eq. (4), the linear terms $h_i \in \mathbb{R}$ and the quadratic couplers $Q_{ij} \in \mathbb{R}$ are chosen by the user to define the problem under investigation. The variables $a_1, \dots, a_n \in \mathbb{B}$ are binary and unknown. The aim is to find a configuration of a_1, \dots, a_n which minimizes eq. (4).

Quantum annealing is based on adiabatic quantum computation, where the system is initialized in the ground state of a Hamiltonian that is easy to prepare, in the case of D-Wave this is the transverse field Hamiltonian. The system is then slowly transitioned to a Hamiltonian of interest, whose ground state is unknown (and, likely hard to find). In ideal adiabatic settings, namely if the transition is sufficiently slow, the system will remain in the ground state, leading to the ground state of the final Hamiltonian. Therefore, this can be used as a method of computing ground states of spin systems (Ising models). The system is described as

$$H_{\text{system}}(t) = A(t)H_{\text{init}} + B(t)H_{\text{problem}}, \quad (5)$$

where $A(t)$ and $B(t)$ define the anneal schedule, H_{init} is the transverse field Hamiltonian, and H_{problem} is the problem Ising model that we wish to find the optimal solution of. Ising models can easily be converted into QUBOs, and vice versa, and since many optimization problems can be formulated as QUBOs, quantum annealing can be used to sample solutions of a large number of optimization problems [39, 57].

The physical spin system that the programmable quantum annealers created by D-Wave implement is defined specifically as

$$H_{\text{system}} = -\frac{A(s)}{2} \left(\sum_i^n \sigma_i^x \right) + \frac{B(s)}{2} \left(H_{\text{problem}} \right), \quad (6)$$

where $s \in [0, 1]$ is a variable called the *anneal fraction* which defines a weighting of both the transverse field and problem Hamiltonians (by $A(s)$ and $B(s)$) at each point in time during the anneal, σ_i^x is the Pauli matrix acting on each qubit i , H_{problem} is the problem Ising model that we wish to sample low energy states from. In our case, H_{problem} is the QUBO of eq. (4) that has been converted to an Ising model such that all of the variable states are spins. The user can program a variety of additional features on the device, including different anneal schedules and annealing times.

The other D-Wave device feature we use is *reverse quantum annealing*, see Section 2.3.3. Reverse quantum annealing uses a modified anneal schedule where we initialize the system in a classical spin configuration (each variable is either spin up or spin down). Then, we program an anneal schedule that varies the anneal fraction s such that some proportion of the transverse field Hamiltonian is introduced into the system, up until the system state is measured (at which point, the anneal fraction must be $s = 1$).

The workflow for using the D-Wave quantum annealer is described in the following sections. All quantum annealing results presented in this article were computed on the D-Wave `Advantage.system4.1` device. The device-specific values for $A(s)$ and $B(s)$ on `Advantage.system4.1` are given in Appendix B.

2.3.1 Parallel Quantum Annealing Minor Embeddings

D-Wave `Advantage.system4.1` has a logical hardware graph (the connectivity graph of the physical hardware qubits on the QPU) that is called Pegasus [8, 58, 16]. Due to manufacturing defects, the chip does not have the full yield of intended hardware qubits and couplers compared to the logical Pegasus graph. The device has 5627 programmable qubits and 40279 couplers which allow for tunable interactions between qubits.

Normally, the connectivity graph of the logical qubits in eq. (4) does not match the one of the hardware qubits on the D-Wave QPU. In this case, a minor embedding of the problem onto the hardware architecture is necessary. The idea is to represent logical variable states by a path of qubits on the hardware graph (that are connected on the hardware graph), where the couplers between those qubits are bound with ferromagnetic links so that their spin states are incentivized to be the same (specifically, they are penalized via an energy penalty if the spins disagree) [9, 10, 54, 58, 12, 53]. These paths of physical qubits are called *chains*, and they are intended to encode the logical variable state of one of the variables in the original QUBO problem.

In order to make more effective use of the large hardware graph of D-Wave’s `Advantage.system4.1` (compared to the QUBO models which are being embedded), we employ *parallel quantum annealing*, also *tiling*, in which multiple Ising models can be embedded on the chip such that they are disjoint and are solved in parallel during a single anneal [43, 44, 1]. As shown in Figure 6, we use multiple all-to-all minor embeddings onto the D-Wave hardware graph, thus allowing us to solve the same problem multiple times simultaneously during a single anneal readout cycle. This allows us to obtain more samples per anneal, but also mitigates local biases and errors that may be present on some parts of the chip (as well as differences in the random minor-embeddings). Moreover, parallel quantum annealing partially mitigates the effects of using a single sub-optimal embedding due to multiple different random embeddings being used, and also different parts of the hardware graph being used (since the D-Wave hardware has non-uniform noise properties across the different components). Note that parallel quantum annealing is also referred to as *tiling* in the D-Wave documentation¹. Throughout all experiments, we consider all-to-all embeddings for sizes 64 and 128 variables. Those minor embeddings can be computed with the heuristic tool `minorminer` [12], applied iteratively to the hardware graph in order to obtain disjoint minor embeddings, using the methods described in [43] which attempts to maximize the number of disjoint minor embeddings that can be embedded on the hardware graph.

Figure 6 in Appendix A shows an example of two such embeddings. The first example shown in Figure 6 visualizes seven disjoint minor embeddings of size 64 variables, the second shows two disjoint minor embeddings of size 128, each time with all-to-all connectivity. Note that these visualizations of the embeddings are intended to show what regions of the chip are being used. In the plots, all edges and nodes which are present in the induced subgraph are being shown, although the actual minor embeddings might have a sparser connectivity structure.

2.3.2 Choice of D-Wave parameters

With newer generations of the D-Wave quantum annealers, more and more features have been added which give the user a greater control over the anneal process. The specific parameters being used are listed in this section.

One necessary consequence of the minor embeddings are the presence of chains, that is the representation of a logical qubit as a set of physical hardware qubits on the chip. However, after annealing, it is not guaranteed that all the physical qubits in a chain take the same value (either zero or one), although they technically represent the same logical qubit. Such a chain is called “broken”. To arrive at a value for the logical qubit in eq. (4), we used the *majority vote* chain break resolution algorithm [53].

We employ the D-Wave annealer with an annealing time of 100 microseconds, and we query 1000 samples per D-Wave backend call. To compute the chain strength, we employ the uniform torque compensation feature with a UTC prefactor of 0.6. The UTC computation, given a problem QUBO, attempts to compute a chain strength which will minimize chain breaks while not too greatly disrupting the maximum energy scale programmed on the device [14].

For all experiments involving reverse annealing, the schedule used is $\{[0, 1], [10, s], [90, s], [100, 1]\}$, where each tuple defines a point in time (from the start to the end of the anneal process) and an anneal fraction s . The anneal fraction is the normalized time used to control how the quantum Hamiltonian is moved from the initial

¹<https://dwave-systemdocs.readthedocs.io/en/samplers/reference/composites/tiling.html>

superposition of states to the problem QUBO (which is a classical Hamiltonian) during the anneal [11]. The anneal schedule is constructed by linear interpolation between those four points. The reverse anneal schedule we use is symmetric with a pause of 80 microseconds. It has an increasing and decreasing ramp on either side of a pause of duration 10 microseconds. We vary the anneal fraction s at which the pause occurs.

Moreover, we called the D-Wave quantum annealer with flag `reduce_intersample_correlation` enabled for all experiments, which adds a pause in between each anneal so as to reduce self correlations between the anneals (those correlations may exist in time due to the spin bath polarization effect, see [37]). Both parameters `readout_thermalization` and `programming_thermalization` were set to 0 microseconds. The reverse annealing specific parameter `reinitialize_state` was enabled for all reverse annealing executions, causing the annealer to reapply the initial classical state after each anneal readout cycle [13].

2.3.3 Quantum Evolution Monte Carlo with Reverse Annealing

We will use the D-Wave annealer in connection with a Monte Carlo chain of reverse anneals, in which the best solution of an initial set of anneal-readout cycles is encoded as the initial state of the next anneal, and then the best solutions found from each iteration are used as the initialized classical spin state of the subsequent (reverse) anneals. This process works on the *logical* problem, meaning after unembedding of all chained qubits.

To be precise, a sequence of reverse anneals are chained together in a Monte Carlo like process, where each subsequent round of reverse anneals is initialized with a classical state that is defined by the best solution found at the last set of reverse anneals. This chain of reverse anneals is initialized with the best solution found from a 100 microsecond forward anneal with 1000 samples and the standard linear anneal schedule (forward anneal denotes that it is a standard annealing process, initialized in a uniform superposition and not in a specific configuration of spins). Because of the use of parallel quantum annealing, there is a multiplier on the total number of samples obtained at each QEMC step; for the 64 variable QUBO problems we actually obtain 7,000 samples per 1,000 sample anneal readout cycle, and for the 128 variable QUBO problems we obtain 2,000 samples per 1,000 sample anneal readout cycle. Each reverse annealing step in the chain uses the parameter `reinitialize_state=True` when executing on the D-Wave quantum annealers, which re-initializes the state of the reverse anneal after each anneal-readout cycle. This technique has been used in other contexts, and is referred to as both “iterative reverse annealing” [56, 4, 2, 42] and “quantum evolution Monte Carlo” (QEMC) [33, 32, 34, 29, 38]. The technique we use here differs slightly from some of these approaches in that we do not use a single anneal-readout cycle at each step of the Monte Carlo chain process, instead we use a batch of anneals at each step and initialize the next anneal with the lowest energy solution found in the current batch of anneals.

2.4 Simulated Annealing Implementation

Simulated annealing is a classical heuristic algorithm which samples combinatorial optimization problems quite effectively [35]. The QUBO models described in Section 2.1 can directly be sampled using a standard simulated annealing implementation, in this case we use the `dwave-neal` simulated annealing python software ² in order to provide a reasonable basis of comparison between the evaluated algorithms and hardware.

Specifically, we use 1000 reads per QUBO, while all other settings are set to their default values. This means that the annealing schedule is set to `geometric`. This implementation is a fast C++ implementation where a complete sweep of variable updates (Metropolis-Hastings updates) are performed in a fixed order for each temperature in the defined schedule of β values. The range of β values is computed based on the coefficients of the given QUBO problem ³. The parameter β denotes the inverse temperature $\frac{1}{k_B T}$ of the Boltzmann distribution, where k_B is the Boltzmann constant and T is the thermodynamic temperature [35]. In the default settings that we use, 1000 Metropolis-Hastings updates are performed for each sample (where each update uses a different β defined by the schedule, and each β is utilized only once).

2.5 Exact QUBO solutions using CPLEX

In order to determine how well all of the evaluated heuristic methods worked at sampling the optimal solution(s) of the generated QUBO models, we used the classical CPLEX [25] solver which can solve the generated QUBOs exactly. To this end, we first transform each QUBO into a Mixed Integer Quadratic Programming (MIQP) problem, and solve those problems exactly using the CPLEX solver [25]. The CPLEX solver does not provide information on whether the QUBOs have multiple optimal solutions, or only 1, however it is expected that in general these

²<https://github.com/dwavesystems/dwave-neal>

³<https://github.com/dwavesystems/dwave-neal/blob/master/neal/sampler.py>

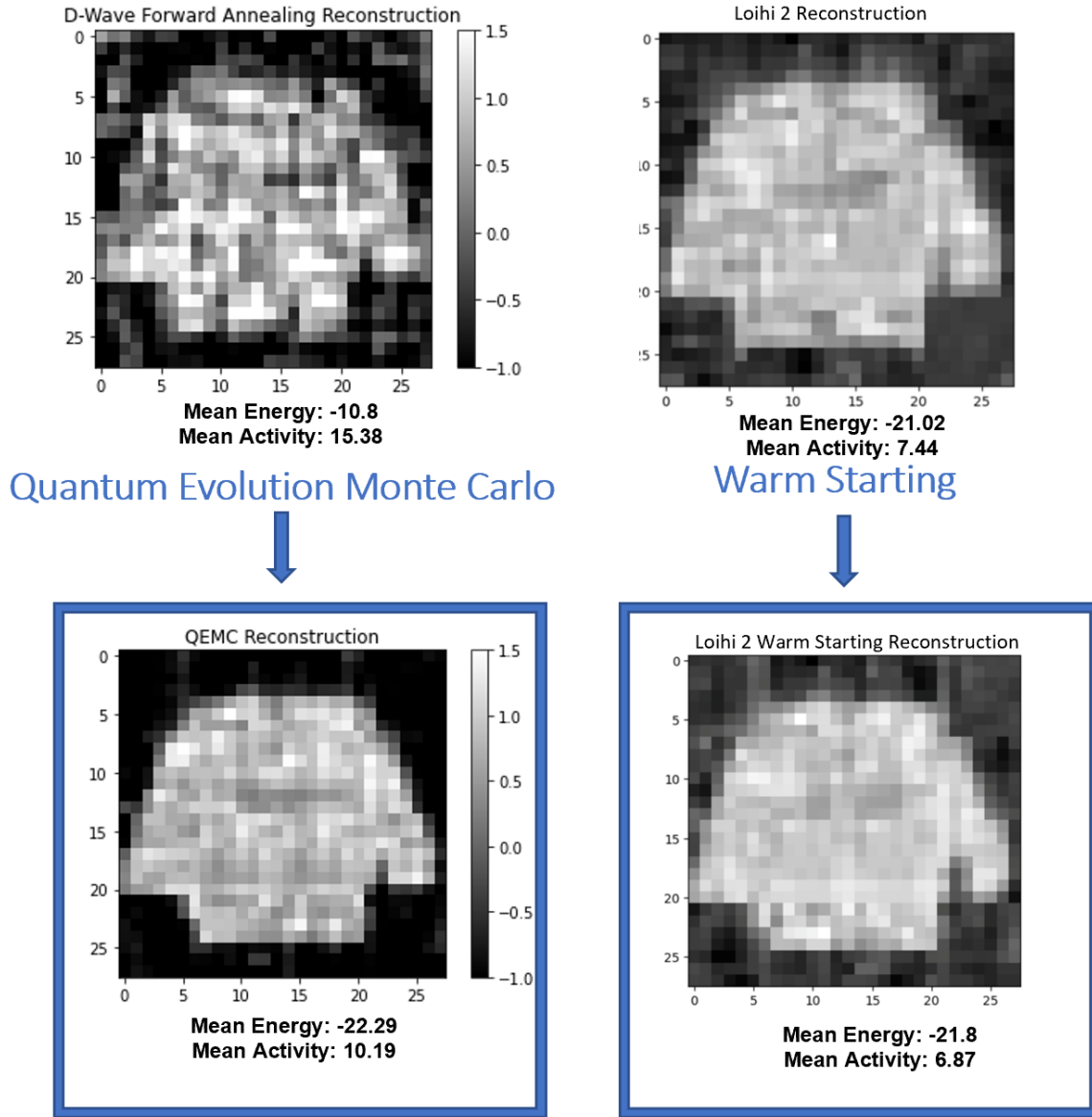


Figure 2: Top: The best (lowest energy) reconstruction found using D-Wave with standard forward annealing (with no parallel QA and a default annealing time of 20 microseconds), reverse annealing QEMC, neuromorphic computing on Loihi 2, and iterated warm starting neuromorphic computing with Loihi 2 (in order). Below: Experimentally computed figure reconstructions are the best mean energy and best mean sparsity across the 16 QUBO models (for the best parameter combination found for each device or technique).

QUBOs will not have degenerate ground states. We leave further investigations on the ground state degeneracy of these binary sparse coding QUBO problems to future research.

3 Results

Figure 2 shows the combined best image reconstruction from sampling the 16 QUBOs using the 4 different methods. We observe that Loihi 2 provides a better first solution and has slight improvement with warm starting, while standard forward annealing is initially very poor, but achieves better average final solutions when reverse annealing QEMC is used.

Figure 3 presents the iterated warm started learning on Loihi 2 for all 16 of the 64 decision variable QUBO models. Interestingly, this process of warm starting the simulation using the state found during the previous

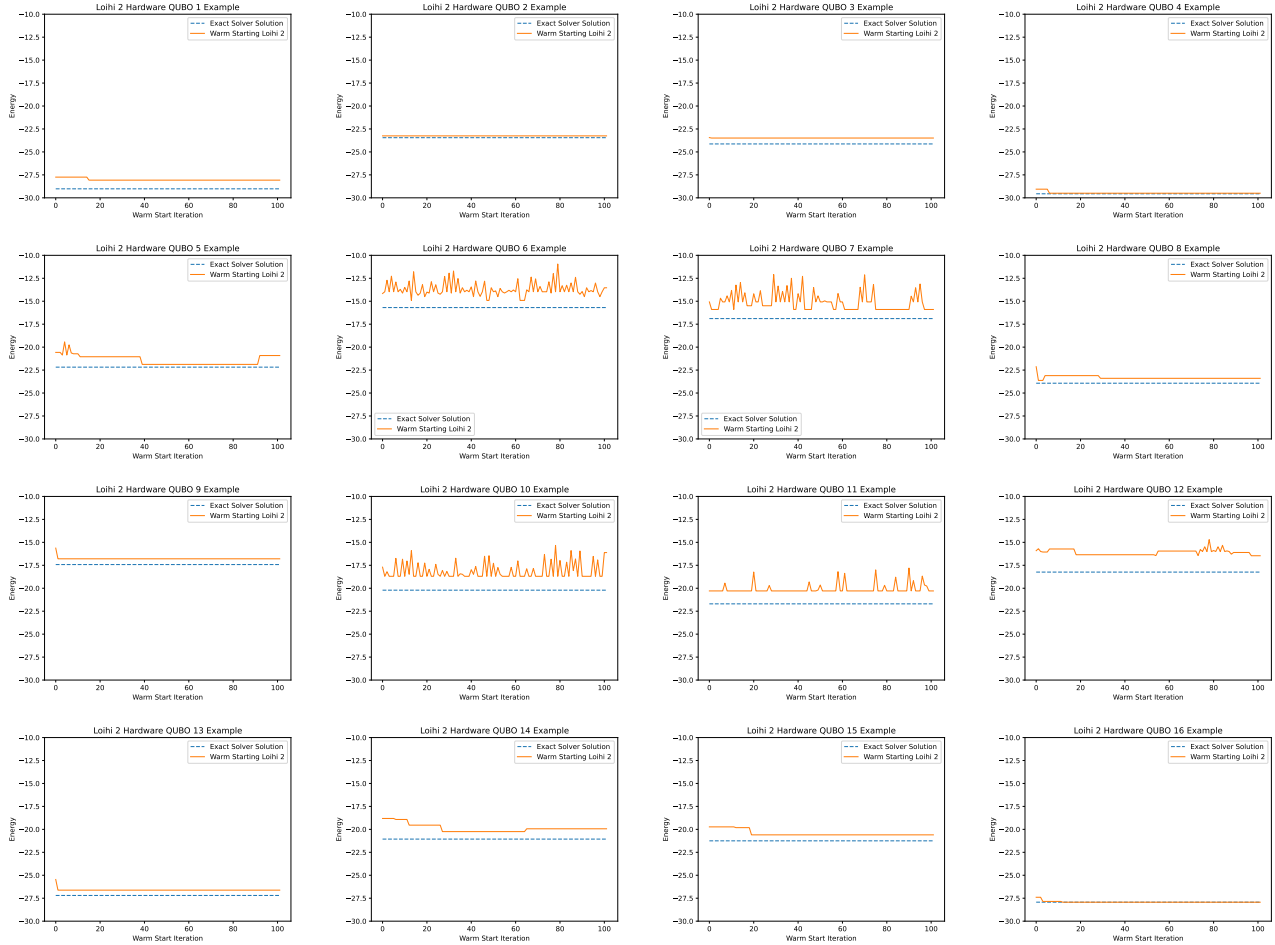


Figure 3: Iterated warm starting on results on Loihi 2 for 100 iterations for each of the 16 QUBO problems (each QUBO contains 64 variables). The minimum energy sample from the converged simulation is plotted at each iteration step.

computation seems to converge fairly fast to a local minimum for most of the QUBO problems. Notably, 4 of the plots show high variability of the learning curve for those QUBOs, whereas for most of the other QUBOs there is very little variability of the learning curve. Figure 3 also plots the minimum energies computed using CPLEX. These results are the first that we are aware of for using iterated warm starting on a spiking neuromorphic processor.

Figure 4 shows the QEMC, or iterated reverse annealing, progression when sampling all of the 16 sparse coding QUBOs using 100 iterations and varying anneal fractions at which the pause occurred. At each QEMC step, the minimum energy (e.g., the objective function evaluation) sample is plotted. Figure 4 shows that there are some anneal fractions (s) that produced the desired monotonic decrease of minimum computed energy at each QEMC step, whereas other anneal fractions did not consistently improve on solution quality. Specifically, the anneal fraction of $s = 0.44$ clearly introduced too much of the transverse field Hamiltonian into each simulation, resulting in a loss of information on the best previous obtained solution. On the other hand, the choice $s = 0.6$ did not utilize enough of the quantum fluctuations provided by the transverse field Hamiltonian to search for lower energy states, although the improvement was always monotonic. The anneal fractions of $s = 0.5$ and 0.55 showed the best tradeoff in our experiments, allowing for reasonably good exploration of the problem search space. Figure 4 shows that the RA QEMC method was able to find the optimal solution for some, but not all of the QUBO problems. This is examined in more detail in Table 1. Figure 4 plots the minimum energy computed by simulated annealing as black horizontal dashed lines, and Table 1 shows that those solutions are also optimal as verified by CPLEX. When executing the QEMC simulations of Figure 4, the initial state was chosen to be the best sample found from an initial standard linear schedule forward anneal; that initialization is then repeated with independent anneals for each run of QEMC, meaning that the initial states all have slightly different objective values. If there were multiple solutions with the same objective value, one was chosen arbitrarily as the initial vector.

The ordering of the sub-plots (in terms of the QUBO problem being solved) in Figure 3 and Figure 4 is consistent between the two figures. Notably, all of the iterated reverse annealing plots of Figure 4 show very clear and consistent convergence behavior (e.g. for $s = 0.5$), but the iterated warm starting on Loihi 2 does not have as clear convergence behavior as a function of the iteration index.

Table 1 also reports the sparsity of the optimal bitstring computed by CPLEX. Simulated annealing always correctly found the optimal solution. Loihi 1 found the optimal solution in 0 out of the 16 QUBOs, so the optimal solution count is not shown. The Loihi 1 results are shown for comparison against Loihi 2, and are taken from the simulations in [24], where the minimum energies are taken from the distribution of 2000 samples computed across a varied set of device parameters. The minimum energies reported both from iterated reverse quantum annealing and iterated warm starting on Loihi 2 are the minimum energies found from the entirety of the simulation (which, for converged simulations is the last point found after the 100 iterations). The reported minimum energies from Loihi 2 are taken from the distribution of 100 samples obtained from the iterated warm starting procedure.

Table 1 verifies that the trained sparse coding QUBOs indeed have solution vectors that are reasonably sparse. However, although unlikely to occur for our types of QUBO models, there could exist multiple variable assignments that give the same optimal objective function value (i.e., degenerate ground states). Moreover, as CPLEX only returns one optimal solution, the reported CPLEX results do not capture the case of more than one optimal solution with different sparsity.

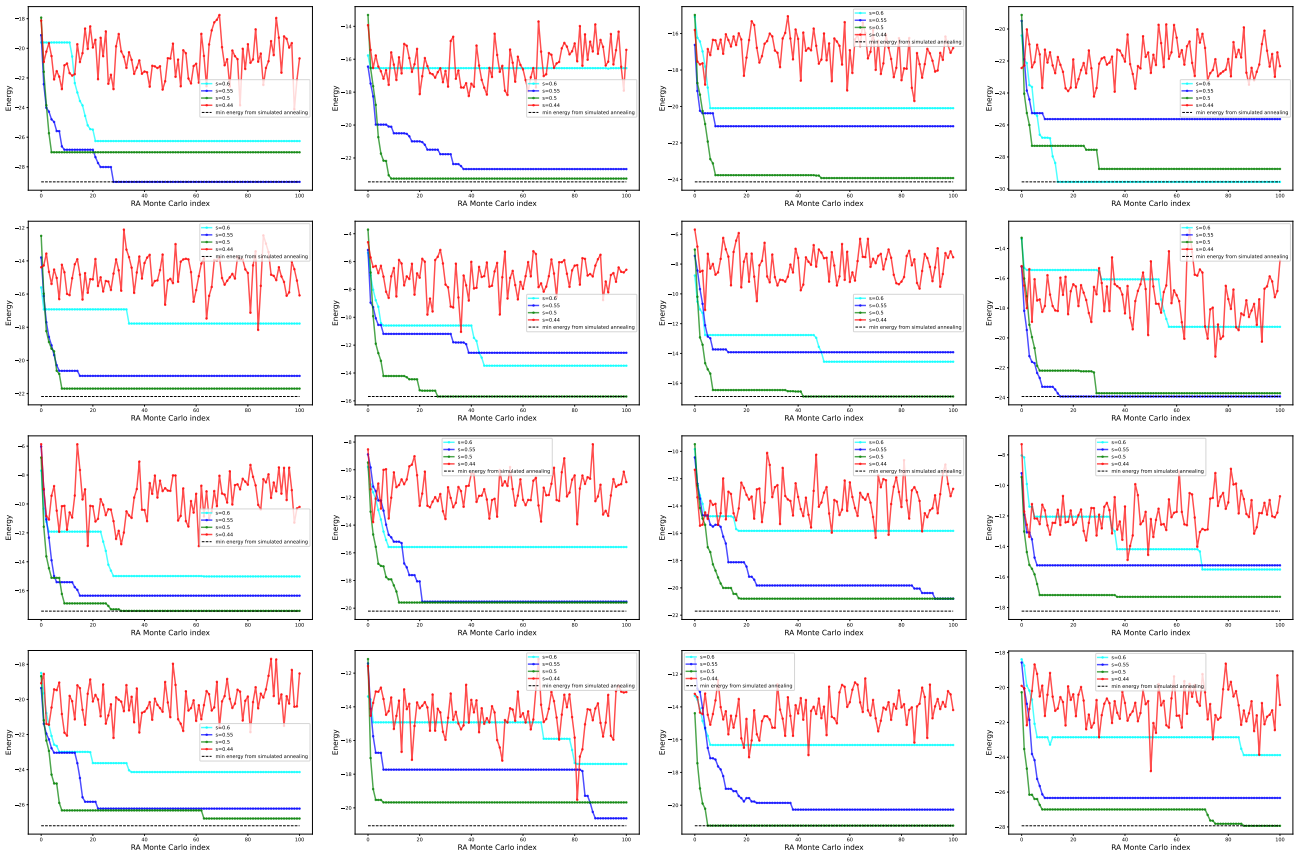


Figure 4: Quantum Evolution Monte Carlo with reverse annealing, where the results for each of the 16 QUBO problems (each QUBO contains 64 variables) is shown by each sub-figure. The anneal fraction at which the reverse anneal is paused is varied, and the resulting minimum energy found in the 1000 samples at each Monte Carlo step is plotted. All quantum annealing computations used an annealing time of 100 microseconds.

3.1 Binary Sparse Coding on 128 variables with QEMC

Figure 5 shows the reverse annealing QEMC protocol applied to 128 variable binary sparse coding QUBOs. These 128 variable QUBOs are generated using the same fMNIST image as the 64 variable QUBO partitioning reconstruction, but in this case the image is partitioned into 4 QUBO models instead of 16. The disjoint minor embeddings

QUBO index	Ground state energy (CPLEX)	Optimal solution sparsity (CPLEX)	SA min. energy	SA min. energy count	QA QEMC min. energy	QA min. energy count	QEMC energy	Loihi 1 min. energy	Loihi 2 iterated warm starting min. energy
0	-29.016	6/64	-29.016	826/1000	-29.016	394186/400000	-26.308	-28.0741	
1	-23.4522	12/64	-23.4522	25/1000	-23.2522	47038/400000	-10.624	-23.2522	
2	-24.1331	9/64	-24.1331	44/1000	-23.9252	20165/400000	-15.784	-23.4876	
3	-29.5586	8/64	-29.5586	117/1000	-29.5586	572222/400000	-29.206	-29.4979	
4	-22.1755	10/64	-22.1755	95/1000	-21.6989	14738/400000	-15.369	-21.8805	
5	-15.6869	10/64	-15.6869	26/10000	-15.6869	14816/400000	-13.188	-14.9114	
6	-16.8891	9/64	-16.8891	123/1000	-16.8891	10487/400000	-12.744	-15.8988	
7	-23.9319	9/64	-23.9319	103/1000	-23.9319	342411/400000	-15.602	-23.6264	
8	-17.416	10/64	-17.416	19/1000	-17.3972	11835/400000	-13.432	-16.7931	
9	-20.2117	7/64	-20.2117	45/1000	-19.591	16110/400000	-16.036	-18.6999	
10	-21.703	7/64	-21.703	41/1000	-20.7899	49428/400000	-18.182	-20.2913	
11	-18.2355	11/64	-18.2355	13/1000	-17.2995	13251/400000	-8.9072	-16.4587	
12	-27.2012	10/64	-27.2012	97/1000	-26.7890	24604/400000	-21.610	-26.621	
13	-21.0627	13/64	-21.0627	66/1000	-20.6227	59717/400000	-8.747	-20.2434	
14	-21.254	11/64	-21.254	29/1000	-21.2437	90453/400000	-8.771	-20.5983	
15	-27.9347	5/64	-27.9347	266/1000	-27.9347	14957/400000	-26.593	-27.9347	

Table 1: Optimal solutions and the best solutions found by simulated annealing, quantum annealing, and Loihi 2 for each of the 16 QUBO problems (each QUBO contains 64 variables). Objective function evaluations (e.g., energies) are rounded to a precision of 4 decimal places. The optimal solution sparsity is a fraction out of 64, which shows how many of the variables are in a 1 state. The RA QEMC sampling ground state energy success proportion is out of all samples (including parallel QA samples) across all parameter choices that were tested (specifically, the 4 different anneal fractions at which the pause was set).

used for the 128 RA QEMC procedure is shown in Figure 6 (right), where only 2 of the all-to-all random minor embeddings could be tiled. In Figure 5, we see that QEMC fails to reach the solutions that simulated annealing finds. This is notable because it shows a very different performance compared to the 64 variable QUBO problems. However, these results are consistent with the properties of minor embeddings with necessarily longer chains (in particular, resulting in higher chain break rates), especially considering the encoding precision requirements for these binary sparse coding QUBO problems.

Both Figure 4 and 5 show that iterating reverse annealing, applied to these fully connected QUBOs, significantly improves the found solutions. In particular, when a good anneal fraction is used for the reverse anneal pause, the solution quality monotonically improves. This is significant to see for such large minor embedded optimization problems. The effectiveness of iterated reverse annealing, or QEMC, has not been empirically demonstrated for minor embedded systems of this size, as far as we are aware.

Like Figure 4, Figure 5 plots the best solution found when executing simulated annealing on the problem QUBOs - and like Figure 4, the simulated annealing solutions are also the optimal solutions found by CPLEX. In other words, the dashed horizontal black line in Figure 5 denotes the optimal energy of, or cost value, of these 128 variable QUBOs.

The best anneal fraction, which tradeoffs between exploration of new solutions and retaining memory of the initial spin state, is usually either 0.5 or 0.55 - and this is true for both Figure 4 and 5. Notably, using a reverse annealing pause at $s = 0.4$ causes the Monte Carlo chain to not converge, but rather to oscillate approximately at the energy of the starting state at the beginning of the process.

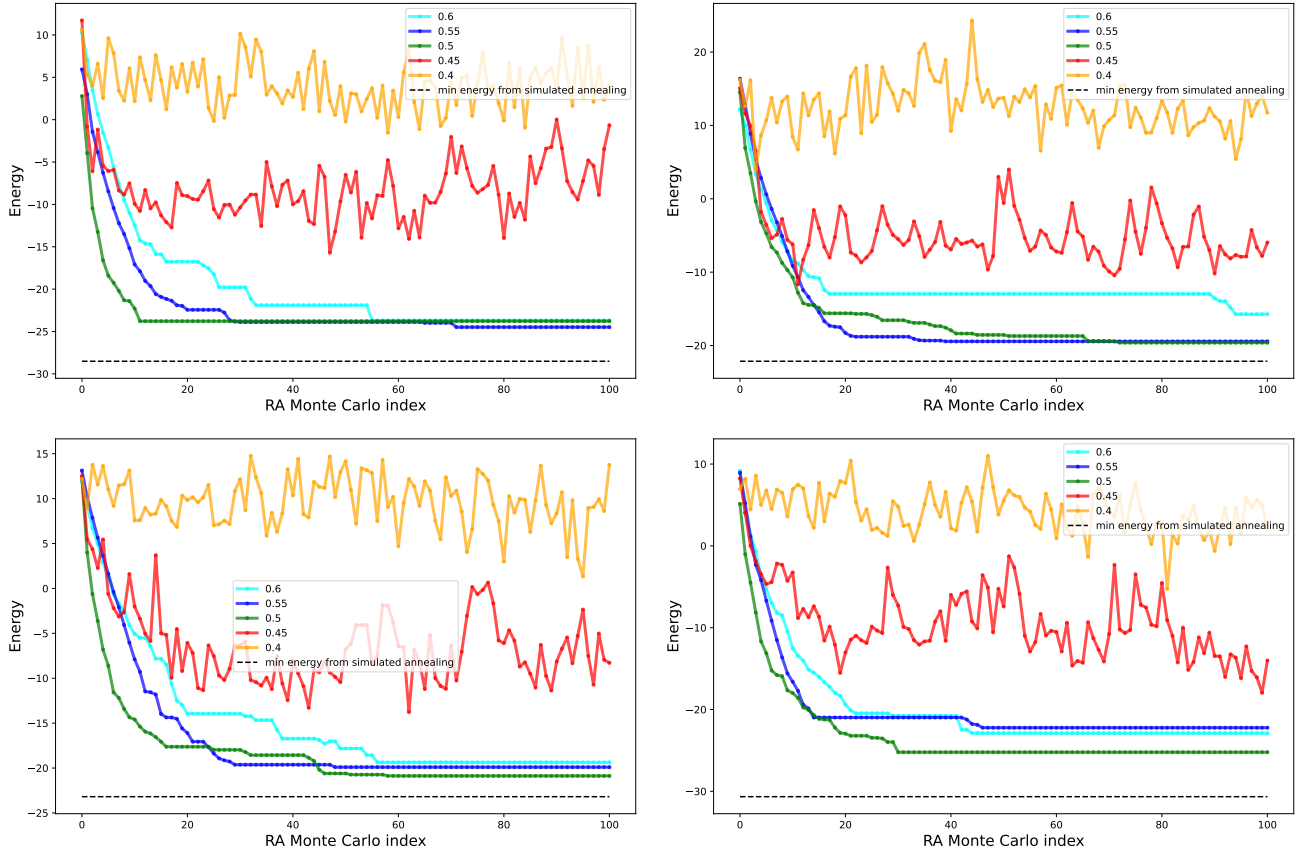


Figure 5: Quantum Evolution Monte Carlo with reverse annealing for 128 variable QUBOs. Each line is plotting the Monte Carlo simulation result minimum energy found (out of the 1000 samples measured at each iteration) for different anneal fractions s at which the anneal is (symmetrically) paused at during reverse annealing.

4 Discussion

In this article we have demonstrated that moderately sized binary sparse coding QUBO models can be sampled using both quantum annealing and neuromorphic computing technologies. These binary sparse coding QUBO problems were constructed using an un-supervised and un-normalized dictionary learning approach. We have found that the iterated reverse quantum annealing technique, implemented on a D-Wave quantum annealer, performed better than standard forward annealing. Similarly, iterated warm starting on Loihi 2 improved the solution quality of sampling the QUBOs. However, this energy improvement was marginal. We also found that the Loihi 2 sampling was better than the sampling done on Loihi 1 [24]. Notably, a consistent trend for the Loihi processor sampling is that the generated samples tend to be quite sparse – more sparse than sub-optimal sampling from standard simulated annealing or quantum annealing.

Amongst others, the following three reasons might have impeded the forward annealing and reverse annealing sampling from reaching the global minimum in our experiments.

1. The first, and almost certainly the most important, is the coefficient precision limits that can be programmed on current D-Wave devices. The sparse coding QUBOs have quadratic terms which are defined with high precision, and are nearly all very close to zero (see Figure 1). It seems very likely that such sparse coding QUBOs are simply not able to be correctly programmed at the hardware level due to the current limitations of the device.
2. The next obstacle is the use of a minor embedding. A minor embedding is necessary for implementing general QUBO problems on D-Wave, however such embeddings can have ferromagnetic chains which dominate the energy scale programmed on the chip, therefore not allowing a larger range of the logical problem coefficients to be effectively used in the computation. Additionally, although majority vote unembedding is used, chain breaks that are present in the samples represent likely sub-optimal solution quality.

3. Interaction with the environment that can cause biased noise.

For future research, it would be interesting to be able to formulate sparse coding QUBO problems that match a desired connectivity graph. This would be particularly useful for generating hardware-compatible QUBOs for D-Wave hardware graphs, as it would allow one to considerably scale up the size of QUBO problems that can be solved (up to the size of the entire hardware graph, which has over 5000 qubits). In particular, probing the scaling of solution quality for future generations of both neuromorphic processors and quantum annealing processors would be of interest to compare against existing classical methods.

A Parallel Minor Embeddings

Figure 6 shows the parallel minor embeddings on the Pegasus hardware graph.

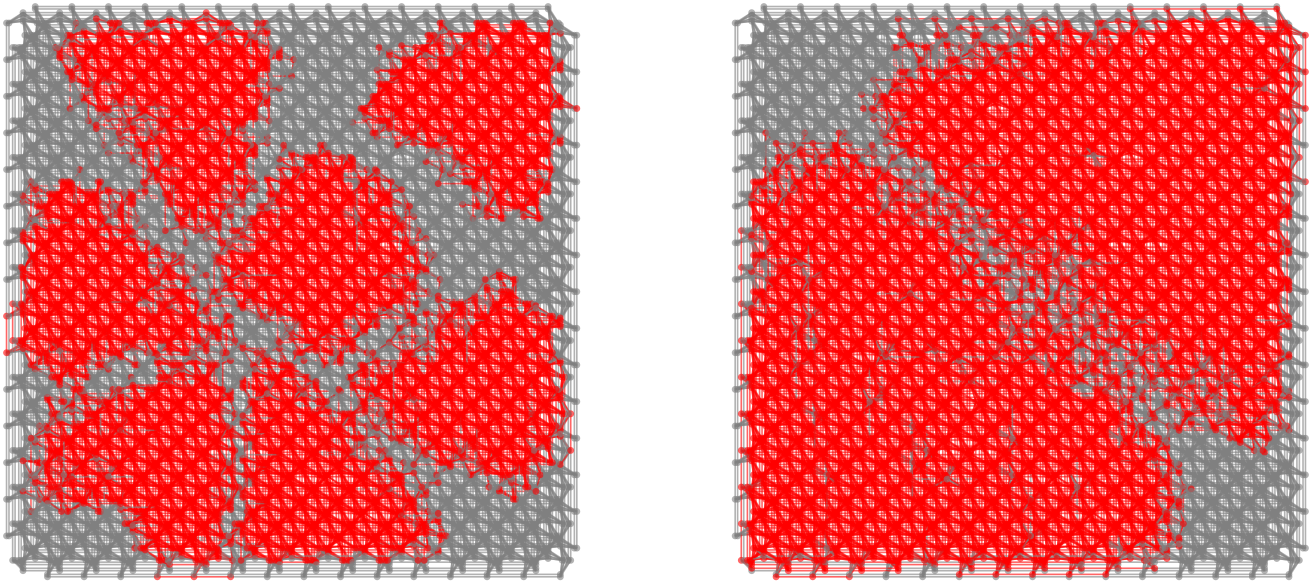


Figure 6: Seven disjoint minor embeddings of size 64 variables with all-to-all connectivity (left), and two disjoint minor embeddings of size 128 variables with all-to-all connectivity (right) on the Pegasus P_{16} hardware graph of the Advantage_system4.1.

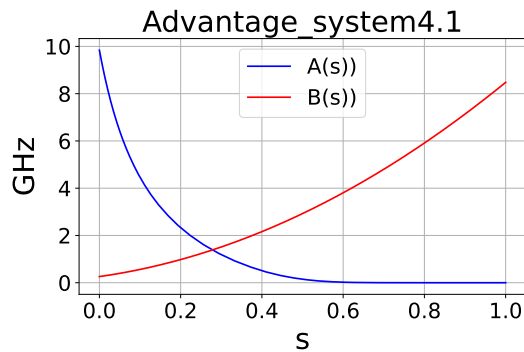


Figure 7: Schedule calibration for the exact $A(s)$ and $B(s)$ values in terms of GHz as a function of the anneal fraction $s \in [0, 1]$.

B D-Wave Quantum Annealer Schedule Calibration

Figure 7 gives the exact vendor-provided anneal schedule calibration data.

Acknowledgments

This work was supported by the U.S. Department of Energy through Los Alamos National Laboratory. Los Alamos National Laboratory is operated by Triad National Security, LLC, for the National Nuclear Security Administration of the U.S. Department of Energy (under the contract No. 89233218CNA000001). The research presented in this article was supported by the Laboratory Directed Research and Development program of Los Alamos National Laboratory under the project number 20220656ER. This research used resources (D-Wave Leap Cloud access) provided by the Los Alamos National Laboratory Institutional Computing Program, which is supported by the U.S. Department of Energy National Nuclear Security Administration under Contract No. 89233218CNA000001. Research presented in this article was supported by the NNSA’s Advanced Simulation and Computing Beyond Moore’s Law Program at Los Alamos National Laboratory. We gratefully acknowledge support from the Advanced Scientific Computing Research (ASCR) program office in the Department of Energy’s (DOE) Office of Science, award #77902. This research used resources provided by the Darwin testbed at Los Alamos National Laboratory (LANL) which is funded by the Computational Systems and Software Environments subprogram of LANL’s Advanced Simulation and Computing program (NNSA/DOE). This paper has been assigned LANL report number LA-UR-23-26361

References

- [1] Tameem Albash et al. “Consistency tests of classical and quantum models for a quantum annealer”. In: *Phys. Rev. A* 91 (4 2015), p. 042314. DOI: 10.1103/PhysRevA.91.042314. URL: <https://link.aps.org/doi/10.1103/PhysRevA.91.042314>.
- [2] Shunta Arai, Masayuki Ohzeki, and Kazuyuki Tanaka. “Mean field analysis of reverse annealing for code-division multiple-access multiuser detection”. In: *Phys Rev Research* 3 (3 2021), p. 033006. DOI: 10.1103/PhysRevResearch.3.033006.
- [3] Ramin Ayanzadeh et al. *Quantum Annealing Based Binary Compressive Sensing with Matrix Uncertainty*. arXiv:1901.00088. 2019.
- [4] Yuki Bando et al. “Breakdown of the Weak-Coupling Limit in Quantum Annealing”. In: *Phys Rev Applied* 17 (5 2022), p. 054033. DOI: 10.1103/PhysRevApplied.17.054033.
- [5] Humberto Munoz Bauza and Daniel A. Lidar. *Scaling Advantage in Approximate Optimization with Quantum Annealing*. 2024. arXiv: 2401.07184 [quant-ph].
- [6] Sergio Boixo et al. “Evidence for quantum annealing with more than one hundred qubits”. In: *Nature Physics* 10.3 (2014), pp. 218–224. DOI: 10.1038/nphys2900. URL: <https://doi.org/10.1038/nphys2900>.
- [7] Sergio Boixo et al. “Experimental signature of programmable quantum annealing”. In: *Nature communications* 4.1 (2013), p. 2067. DOI: 10.1038/ncomms3067.
- [8] Kelly Boothby et al. *Next-Generation Topology of D-Wave Quantum Processors*. arXiv:2003.00133. 2020.
- [9] Vicky Choi. “Minor-embedding in adiabatic quantum computation: I. The parameter setting problem”. In: *Quantum Information Processing* 7 (2008), pp. 193–209.
- [10] Vicky Choi. “Minor-embedding in adiabatic quantum computation: II. Minor-universal graph design”. In: *Quantum Information Processing* 10.3 (2011), pp. 343–353.
- [11] D-Wave Systems. *D-Wave Ocean Software Documentation: Annealing Implementation and Controls*. https://docs.dwavesys.com/docs/latest/c_qpu_annealing.html. 2023.
- [12] D-Wave Systems. *D-Wave Ocean Software Documentation: Minorminer*. <https://docs.ocean.dwavesys.com/projects/minorminer/en/latest/>. 2017.
- [13] D-Wave Systems. *D-Wave Ocean Software Documentation: Solver Parameters*. https://docs.dwavesys.com/docs/latest/c_solver_parameters.html. 2023.
- [14] D-Wave Systems. *D-Wave Ocean Software Documentation: Uniform Torque Compensation*. https://docs.ocean.dwavesys.com/projects/system/en/stable/reference/generated/dwave.embedding.chain_strength.uniform_torque_compensation.html. 2018.
- [15] Arnab Das and Bikas K Chakrabarti. “Colloquium: Quantum annealing and analog quantum computation”. In: *Reviews of Modern Physics* 80.3 (2008), p. 1061. DOI: 10.1103/revmodphys.80.1061.
- [16] Nike Dattani, Szilard Szalay, and Nick Chancellor. *Pegasus: The second connectivity graph for large-scale quantum annealing hardware*. arXiv:1901.07636. 2019.
- [17] Mike Davies et al. “Advancing Neuromorphic Computing With Loihi: A Survey of Results and Outlook”. In: *Proceedings of the IEEE* 109.5 (2021), pp. 911–934. DOI: 10.1109/JPROC.2021.3067593.
- [18] Edward Farhi et al. *Quantum Computation by Adiabatic Evolution*. arXiv:quant-ph/0001106. 2000.

- [19] R Harris et al. “Phase transitions in a programmable quantum spin glass simulator”. In: *Science* 361.6398 (2018), pp. 162–165. DOI: 10.1126/science.aat2025.
- [20] Philipp Hauke et al. “Perspectives of quantum annealing: methods and implementations”. In: *Reports on Progress in Physics* 83.5 (2020), p. 054401. DOI: 10.1088/1361-6633/ab85b8. URL: <https://dx.doi.org/10.1088/1361-6633/ab85b8>.
- [21] Kyle Henke, Garrett T. Kenyon, and Ben Migliori. “Fast Post-Hoc Normalization for Brain Inspired Sparse Coding on a Neuromorphic Device”. In: *IEEE Transactions on Parallel and Distributed Systems* 33.2 (2022), pp. 302–309. DOI: 10.1109/TPDS.2021.3068777.
- [22] Kyle Henke, Garrett T. Kenyon, and Ben Migliori. “Machine Learning in a Post Moore’s Law World: Quantum vs. Neuromorphic Substrates”. In: *2020 IEEE Southwest Symposium on Image Analysis and Interpretation (SSIAI)*. 2020, pp. 74–77. DOI: 10.1109/SSIAI49293.2020.9094596.
- [23] Kyle Henke, Ben Migliori, and Garrett T. Kenyon. “Alien vs. Predator: Brain Inspired Sparse Coding Optimization on Neuromorphic and Quantum Devices”. In: *2020 International Conference on Rebooting Computing (ICRC)*. 2020, pp. 26–33. DOI: 10.1109/ICRC2020.2020.00015.
- [24] Kyle Henke et al. “Sampling binary sparse coding QUBO models using a spiking neuromorphic processor”. In: *Proceedings of the 2023 International Conference on Neuromorphic Systems*. ICONS ’23. ACM, Aug. 2023. DOI: 10.1145/3589737.3606003. arXiv: 2306.01940. URL: <http://dx.doi.org/10.1145/3589737.3606003>.
- [25] IBM ILOG CPLEX. “V12.10.0 : User’s Manual for CPLEX”. In: *International Business Machines Corporation* 46.53 (2019), p. 157.
- [26] Naoki Ide and Masayuki Ohzeki. *Sparse Signal Reconstruction with QUBO Formulation in l0-regularized Linear Regression*. arXiv:2202.00452. 2022.
- [27] Mark W Johnson et al. “Quantum annealing with manufactured spins”. In: *Nature* 473.7346 (2011), pp. 194–198. DOI: 10.1038/nature10012.
- [28] Tadashi Kadowaki and Hidetoshi Nishimori. “Quantum annealing in the transverse Ising model”. In: *Physical Review E* 58.5 (1998), pp. 5355–5363. DOI: 10.1103/physreve.58.5355. URL: <https://doi.org/10.1103/PhysRevE.58.5355>.
- [29] Paul Kairys et al. “Simulating the Shastry-Sutherland Ising Model Using Quantum Annealing”. In: *PRX Quantum* 1 (2 2020), p. 020320. DOI: 10.1103/PRXQuantum.1.020320.
- [30] Andrew D. King et al. “Coherent quantum annealing in a programmable 2,000 qubit Ising chain”. In: *Nature Physics* 18.11 (2022), pp. 1324–1328. DOI: 10.1038/s41567-022-01741-6. URL: <https://doi.org/10.1038/s41567-022-01741-6>.
- [31] Andrew D. King et al. *Computational supremacy in quantum simulation*. 2024. arXiv: 2403.00910 [quant-ph].
- [32] Andrew D. King et al. “Observation of topological phenomena in a programmable lattice of 1,800 qubits”. In: *Nature* 560.7719 (2018), pp. 456–460. DOI: 10.1038/s41586-018-0410-x.
- [33] Andrew D. King et al. “Quantum Annealing Simulation of Out-of-Equilibrium Magnetization in a Spin-Chain Compound”. In: *PRX Quantum* 2.3 (2021). DOI: 10.1103/prxquantum.2.030317.
- [34] Andrew D. King et al. “Scaling advantage over path-integral Monte Carlo in quantum simulation of geometrically frustrated magnets”. In: *Nature Communications* 12.1 (2021). DOI: 10.1038/s41467-021-20901-5.
- [35] Scott Kirkpatrick, C Daniel Gelatt Jr, and Mario P Vecchi. “Optimization by simulated annealing”. In: *science* 220.4598 (1983), pp. 671–680. DOI: 10.1126/science.220.4598.671.
- [36] T. Lanting et al. “Entanglement in a Quantum Annealing Processor”. In: *Physical Review X* 4.2 (2014). DOI: 10.1103/physrevx.4.021041. URL: <https://doi.org/10.1103/PhysRevX.4.021041>.
- [37] T. Lanting et al. *Probing Environmental Spin Polarization with Superconducting Flux Qubits*. 2020. arXiv: 2003.14244 [quant-ph].
- [38] Alejandro Lopez-Bezanilla et al. *Kagome qubit ice*. arXiv:2301.01853. 2023.
- [39] A. Lucas. “Ising formulations of many NP problems”. In: *Front Phys* 2.5 (2014), pp. 1–27.
- [40] Rahul Mohideen, Pascal Peter, and Joachim Weickert. “A systematic evaluation of coding strategies for sparse binary images”. In: *Signal Processing Image Communication* 99 (2021), p. 116424.
- [41] Satoshi Morita and Hidetoshi Nishimori. “Mathematical foundation of quantum annealing”. In: *Journal of Mathematical Physics* 49.12 (2008), p. 125210. DOI: 10.1063/1.2995837.
- [42] Elijah Pelofske, Georg Hahn, and Hristo Djidjev. “Initial State Encoding via Reverse Quantum Annealing and H-Gain Features”. In: *IEEE Transactions on Quantum Engineering* 4 (2023), pp. 1–21. ISSN: 2689-1808. DOI: 10.1109/tqe.2023.3319586. arXiv: 2303.13748. URL: <http://dx.doi.org/10.1109/TQE.2023.3319586>.
- [43] Elijah Pelofske, Georg Hahn, and Hristo N Djidjev. “Parallel Quantum Annealing”. In: *Scientific Reports* 12.1 (2022), pp. 1–11. DOI: 10.1038/s41598-022-08394-8.

- [44] Elijah Pelofske, Georg Hahn, and Hristo N. Djidjev. “Solving Larger Maximum Clique Problems Using Parallel Quantum Annealing”. In: *Quantum Information Processing* 22.5 (May 2023). ISSN: 1573-1332. DOI: 10.1007/s11128-023-03962-x. URL: <http://dx.doi.org/10.1007/s11128-023-03962-x>.
- [45] Yaniv Romano et al. *Quantum Sparse Coding*. arXiv:2209.03788. 2022.
- [46] Christopher J Rozell et al. “Sparse coding via thresholding and local competition in neural circuits”. In: *Neural computation* 20.10 (2008), pp. 2526–2563.
- [47] Giuseppe E Santoro and Erio Tosatti. “Optimization using quantum mechanics: quantum annealing through adiabatic evolution”. In: *Journal of Physics A: Mathematical and General* 39.36 (2006), R393. DOI: 10.1088/0305-4470/39/36/R01.
- [48] Catherine D Schuman et al. “Opportunities for neuromorphic computing algorithms and applications”. In: *Nature Computational Science* 2.1 (2022), pp. 10–19. DOI: 10.1038/s43588-021-00184-y.
- [49] Byron Tasseff et al. *On the Emerging Potential of Quantum Annealing Hardware for Combinatorial Optimization*. arXiv:2210.04291. 2022.
- [50] R. Tibshirani. “Regression Shrinkage and Selection Via the Lasso”. In: *J Roy Stat Soc B Met* 58.1 (1996), pp. 267–288. DOI: 10.1111/j.1467-9868.2011.00771.x.
- [51] M. Ting, R. Raich, and A. Hero. “Sparse Image Reconstruction using Sparse Priors”. In: *International Conference on Image Processing, Atlanta, GA, USA*. 2006, pp. 1261–1264. DOI: 10.1109/ICIP.2006.312574.
- [52] Joel A. Tropp and Anna C. Gilbert. “Signal Recovery From Random Measurements Via Orthogonal Matching Pursuit”. In: *IEEE Transactions on Information Theory* 53.12 (2007), pp. 4655–4666. DOI: 10.1109/TIT.2007.909108.
- [53] Davide Venturelli et al. “Quantum Optimization of Fully Connected Spin Glasses”. In: *Physical Review X* 5.3 (2015). DOI: 10.1103/physrevx.5.031040. URL: <https://doi.org/10.1103/physrevx.5.031040>.
- [54] Walter Vinci et al. “Quantum annealing correction with minor embedding”. In: *Phys. Rev. A* 92 (4 2015), p. 042310. DOI: 10.1103/PhysRevA.92.042310. URL: <https://link.aps.org/doi/10.1103/PhysRevA.92.042310>.
- [55] Han Xiao, Kashif Rasul, and Roland Vollgraf. *Fashion-MNIST: a Novel Image Dataset for Benchmarking Machine Learning Algorithms*. 2017. URL: <http://arxiv.org/abs/1708.07747>.
- [56] Yu Yamashiro et al. “Dynamics of reverse annealing for the fully connected p -spin model”. In: *Phys Rev A* 100 (5 2019), p. 052321. DOI: 10.1103/PhysRevA.100.052321.
- [57] Sheir Yarkoni et al. “Quantum Annealing for Industry Applications: Introduction and Review”. In: *Rep Prog Phys* 85.104001 (2022).
- [58] Stefanie Zbinden et al. “Embedding algorithms for quantum annealers with chimera and pegasus connection topologies”. In: *International Conference on High Performance Computing*. 2020, pp. 187–206.